Direct effects of the small molecule PD-L1 inhibitor BMS-202 on A375 melanoma cells: Anti-tumor activity accompanied by increased mitochondrial function

NIENG ZHANG[1*], FENGLAN FENG[2*], RUONAN DANG[3], XIAOQING ZHAO[4], XINGRONG WANG[1], YUQI YANG[4], JINJIN DENG[5], YUJIE WANG[1], ZHUOFAN WEN[1], WEI MENG[5], XINGLAN HUANG[6], SHUNYING ZHANG[7], YUQIONG DENG[8], CAIFENG HUANG[1], PENG YAN[9], ZHONGRONG LIU[1] and XIPING CHENG[1,2]

[1]Department of Dermatology, The First Affiliated Hospital of Guangzhou Medical University, School of First Clinical Medicine, Guangzhou Medical University, Guangzhou, Guangdong 510120, P.R. China; [2]The Key Laboratory of Advanced Interdisciplinary Studies, The First Affiliated Hospital of Guangzhou Medical University, Guangzhou Medical University, Guangzhou, Guangdong 510120, P.R. China; [3]Department of Chinese Medicine, The First Affiliated Hospital of Guangzhou Medical University, School of First Clinical Medicine, Guangzhou Medical University, Guangzhou, Guangdong 510120, P.R. China; [4]Department of Traditional Chinese Medicine, Institute of Integrated Chinese and Western Medicine of Guangzhou Medical University, Guangzhou, Guangdong 510182, P.R. China; [5]Department of Obstetrics and Gynecology, The First Affiliated Hospital of Guangzhou Medical University, Guangzhou, Guangdong 510120, P.R. China; [6]Department of Dermatology, Guangzhou Twelfth People's Hospital, Guangzhou, Guangdong 510620, P.R China; [7]Department of Dermatology, Songshan Lake Central Hospital of Dongguan City of Southern Medical University, Dongguan, Guangdong 523000, P.R. China; [8]Department of Dermatology, Panyu Maternal and Child Care Service Centre of Guangzhou, Guangzhou, Guangdong 511400, P.R. China; [9]Department of Critical Care Medicine, Guangzhou First People's Hospital, South China University of Technology, Guangzhou, Guangdong 510180, P.R. China

Received November 20, 2024; Accepted May 14, 2025

DOI: 10.3892/mmr.2025.13607

Abstract. The aim of the present study was to investigate the direct effects of BMS-202 on melanoma cells. The small molecule programmed cell death ligand 1 (PD-L1) inhibitor BMS-202 was used to treat A375 melanoma cells. The cell distribution of BMS-202 was examined using low-power and high-resolution confocal microscopy, focusing on its localization in mitochondria. The impact of BMS-202 on mitochondrial gene expression levels, the activity of respiratory chain complexes, and the levels of reactive oxygen species and apoptosis-related genes, including Bax, Bcl-2, PARP and caspase-3, were assessed by quantitative PCR and western blotting. Additionally, tumor cell viability, proliferation, migration and invasion were evaluated *in vitro*, with *in vivo* experiments conducted through the construction of tumor-bearing mouse models and Ki-67 immunohistochemical staining to validate tumor proliferation. The function of mitochondria was inhibited using a pyruvate carrier inhibitor to examine how this affected the action of BMS-202. The results revealed that BMS-202 can inhibit tumor cell function and promote apoptosis. Furthermore, BMS-202 was shown to enter the mitochondria where it may bind to PD-L1 and improve mitochondrial function. By inhibiting mitochondrial function, the antitumor effects of BMS-202 can be enhanced. Overall, the present study provides information on the potential antitumor mechanisms of BMS-202 as well as a theoretical basis for its application in melanoma therapy.

Correspondence to: Dr Xiping Cheng or Dr Zhongrong Liu, Department of Dermatology, The First Affiliated Hospital of Guangzhou Medical University, School of First Clinical Medicine, Guangzhou Medical University, 151-153 Xingang Xi Road, Haizhu, Guangzhou, Guangdong 510120, P.R. China
E-mail: cxplunwenyx@163.com
E-mail: pfzlzr@163.com

*Contributed equally

Key words: melanoma, programmed cell death ligand 1 inhibitor, mitochondria

Introduction

Malignant melanoma (MM) is a prevalent and aggressive skin cancer, the incidence of which has been increasing annually due to factors such as an increasingly aging population and environmental changes (1-3). While early-stage melanoma can be effectively treated with surgical excision, the treatment of advanced melanoma is challenging due to the high recurrence rate of 60-75%. In addition, melanoma has a 5-year survival rate of 30-70% (4-6). These limitations in surgical treatment have led to the search for more effective therapeutic strategies.

Precision-targeted therapies, particularly immune checkpoint inhibitors, have emerged as promising options for improving outcomes in patients with melanoma (7,8). Current research primarily focuses on the way these inhibitors prevent T cells from escaping immune detection, often neglecting their direct effects on tumor cells (9,10). Recent studies, however, have suggested that programmed cell death ligand 1 (PD-L1) inhibitors may exert direct antitumor effects by modulating tumor cell metabolism and mitochondrial function. For example, Yang *et al* (11) revealed that BMS-202 can reprogram mitochondrial respiration in glioblastoma, leading to suppressed malignancy. Furthermore, Xie *et al* (12) identified mitochondrial PD-L1 as a key regulator of mitophagy and chemoresistance. Research on immune checkpoint inhibition still faces several challenges, particularly the frequent issue of resistance, which may arise from tumor-intrinsic mechanisms such as metabolic adaptation or epigenetic alterations (13-15). For example, Wang *et al* (7), Du *et al* (13) and Tang *et al* (16) revealed that mitochondrial oxidative phosphorylation (OXPHOS) upregulation can contribute to programmed cell death protein 1 (PD-1) inhibitor resistance by enhancing tumor cell survival, highlighting the need to target both immune and metabolic pathways. This gap in knowledge highlights the need for a broader exploration of the function of PD-L1 inhibitors, not just in terms of T cell interactions, but also regarding their direct impact on tumor biology. The present study uniquely bridges this gap by investigating the dual role of BMS-202 in immune checkpoint blockade and mitochondrial modulation. Addressing this issue is key for enhancing the efficacy of immunotherapy in melanoma treatment.

PD-L1 inhibitors are an important type of immunosuppressant (7,16). BMS-202 is a small molecule PD-L1 inhibitor that directly binds to PD-L1, effectively blocking the PD-1/PD-L1 pathway. This pathway has a key role in tumor immune evasion and the effectiveness of BMS-202 has been demonstrated in various studies (11,17).

The present study suggested that BMS-202 not only functions as an immune checkpoint inhibitor, but may also have a direct impact on melanoma cells. More specifically, BMS-202 appears to promote cell death while enhancing mitochondrial function in A375 melanoma cells. Given the established association between mitochondrial health and tumor activity (18), it was hypothesized that BMS-202 could exert direct antitumor effects by modulating mitochondrial function in these cells.

The aim of the present study was to explore the direct effects of BMS-202 on melanoma cells and the underlying mechanisms involved. By investigating these interactions, it was anticipated to provide valuable insights into the broader actions of PD-L1 inhibitors and to identify potential new strategies for improving melanoma treatment. A deeper understanding of the direct effects of PD-L1 inhibitors will enrich the understanding of immunotherapy. The present study investigated the effects of BMS-202 on melanoma cells, highlighting the importance of further research to translate these insights into improved clinical outcomes for patients with melanoma.

Materials and methods

Materials. DMEM and 0.25% trypsin/EDTA solution used for cell passing were purchased from Thermo Fisher Scientific, Inc. BMS-202 (cat. no. HY-19745; MedChemExpress) is a non-peptide inhibitor of the PD-1/PD-L1 complex that binds to PD-L1, effectively blocking the interaction between human PD-1 and PD-L1. GW604714X (GW; cat. no. HY-138559; MedChemExpress) is a highly specific inhibitor of the mitochondrial pyruvate carrier, which markedly suppresses mitochondrial respiration. For western blotting, various primary antibodies were used including β-tubulin (1:5,000; cat. no. FD0064, Hangzhou Fude Biotechnology Co., Ltd.), mitochondrial cytochrome *c* oxidase subunit 1 (MT-CO1; 1:1,000; cat. no. ab14705), Bax (1:100; cat. no. ab32503) and Bcl-2 (1:1,000; cat. no. ab182858) (all from Abcam), as well as horseradish peroxidase-conjugated anti-rabbit (1:1,000, cat. no. ab6721) and anti-mouse (1:1,000, cat. no. ab6728) secondary antibodies (both from Abcam). GAPDH (1:10,000; cat. no. 10494-1-AP), Mitochondrially encoded NADH dehydrogenase 4 (MT-ND4; 1:1,000; cat. no. 26736-1-AP) and MT-ND5 (1:1,000; cat. no. 66613-1-Ig) antibodies were obtained from Proteintech Group, Inc. The antibodies against caspase-3 (1:1,000; cat. no. 9662), poly(ADP-ribose) polymerase (PARP; 1:1,000; cat. no. 9542) and cleaved-caspase-3 (1:1,000; cat. no. 9664T) were obtained from Cell Signaling Technology. PD-L1 (1:5,000, cat. no. ET1701-41, https://huabio.cn/products/PD-L1-antibody-ET1701-41) Inc., whereas antibodies used for the immunofluorescence assay, including those against caspase-3 (1:50; cat. no. 66470-2-Ig) and caspase-8 (1:50; cat. no. A19549) were purchased from Proteintech Group, Inc and ABclonal Biotech Co., Ltd., respectively. Additionally, BMS-202 fluorescently labeled with Cy-3 excitation wavelength, 561 nm) from Guangzhou Weihua Biotechnology Co., Ltd. The mitochondrial dye PKMITO DEEP RED was obtained from Nanjing Puhai Jingshan Biotechnology Co., Ltd., while Hoechst 33342 and DAPI were sourced from Beyotime Institute of Biotechnology.

Cell culture. Melanoma A375 cells were acquired from Wuhan Sean Biotechnology Co., Ltd. (cat. no. CL-0014, l) and have already undergone short tandem repeat profiling. The cells were cultured in DMEM containing 10% fetal bovine serum (cat. no. FSP500; Shanghai ExCell Biology, Inc.), and 1% penicillin and streptomycin, and were maintained in a cell culture incubator at 37˚C and 5% CO_2. Cells in the logarithmic growth phase were selected for experimentation.

Cell treatment. Cells were treated with 5 μM BMS-202 and 10 μM GW after adherence, and incubated in a cell culture incubator for 24 h before subsequent experiments. In the IC_{50} assay, cell viability was measured using concentration gradients of 0.3125, 0.625, 1.25, 2.5, 5, 10, 20, and 40 μM for BMS-202, and 0.3125, 0.625, 1.25, 2.5, 5, 10, 20, 40, and 80 μM for GW, with an incubation time of 24 h. In the CCK-8 assay, cells were treated with 5 μM BMS-202 and 10 μM GW604714X, and cell viability was measured every 24 h for a total duration of 120 h.

Cell viability assay. The viability of A375 cells was determined using the Cell Counting Kit-8 (CCK-8) (cat. no. C0038; Beyotime Institute of Biotechnology) assay. Cells were seeded in a 96-well plate at a density of ~5x10^3 cells/cm^2 and then incubated at 37˚C for 24 h. With the exception of

the blank group, 10 μl CCK-8 solution was then added to each well, and the cells were further incubated for 1-2 h. The optical density (OD) values were measured at 450 nm using a microplate reader. This process was used to determine the cell viability under different concentration treatments and to select the optimal experimental concentration for each group.

Western blotting. Total proteins were extracted using lysis buffer [RIPA(cat. no. P0013B; Beyotime Institute of Biotechnology):PMSF (cat. no. P1045; Beyotime Institute of Biotechnology), 100:1] and protein concentration was determined using a BCA quantification kit, the proteins were denatured at 100˚C for 8 min. Briefly, (20 μg protein) of the extracts were loaded onto SDS-polyacrylamide gels (10.0 and 12.5%), separated by electrophoresis and then transferred to PVDF membranes The membranes were blocked with 5% skimmed milk at room temperature for 60 min., and were subsequently incubated with primary antibodies overnight at 4˚C. Next, the membranes were incubated with secondary antibodies at room temperature for 60 min and detected using the Signaler ECL bioluminescence kit (cat. no. P10100; Suzhou Xinsaimei Biotechnology Co., Ltd.). Protein bands were visualized using bioluminescence imaging systems (Syngene). Grayscale values for semi-quantitative analysis were determined using ImageJ (version 1.54; National Institutes of Health).

Reverse transcription-quantitative PCR (RT-qPCR). Total RNA was extracted from cells using the RNA easy kit (cat. no. R701-01; Vazyme Biotech Co., Ltd.,), according to the manufacturer's instructions. This was followed by RT utilizing the HiScript III RT SuperMix for qPCR (cat. no. R323-01; Vazyme Biotech Co., Ltd.). RT-qPCR was performed using the qPCR kit (cat. no. Q711-02; Vazyme Biotech Co., Ltd.). The thermocycling conditions were as follows: initial denaturation at 95˚C for 30 sec; 40 cycles of 95˚C for 5 sec (denaturation) and 60˚C for 30 sec (annealing/extension); melt curve analysis from 65 to 95˚C. Primers were designed based on the gene sequences listed in the NCBI GenBank (hncbi.nlm.nih.gov/), using Primer premier (version 5.0; Premier Biosoft International). The selected primers (5'→3') encompassed those for MT-CO1 (19), forward CTTTTC ACCGTAGGTGGCCT and reverse AGTGGAAGTGGG CTACAACG; MT-CO3 (20), forward, ATGACCCACCAA TCACATGC and reverse, ATCACATGGCTAGGCCGGA; MT-ND4 (21), forward 5'-3' GCCCAAGAACTATCAAAC TCCTGA and reverse 5'-3' CGGCAAGTACTATTGACC CAGC; MT-ND5 (22), forward 5'-3' GGCTACAAGATATCC GCTGCT and reverse 5'-3' AAAGCCGCATAAGAACCA AA; Bax, forward 5'-3' AGAGGATGATTGCCGCCGT and reverse, CAACCACCCTGGTCTTGGATC; Bcl-2, forward GGTGGGGTCATGTGTGTGG and reverse CGGTTCAGG TACTCAGTCATCC; β-actin, forward CTTCGCGGGCGA CGAT and reverse CCACATAGGAATCCTTCTGACC. The qPCR assays were conducted on a CFX2 system (Bio-Rad Laboratories, Inc.). β-actin served as the internal control for normalization, and the relative gene expression levels were quantified using the $2^{-\Delta\Delta Cq}$ method (23), ensuring precise and reliable data analysis.

Detection of mitochondrial respiratory chain complex I and IV, and superoxide dismutase (SOD). Cells were scraped and homogenized using PBS, followed by centrifugation (4˚C, 10,000 x g, 10 min) to collect the supernatant. The protein concentration was determined using a BCA protein assay kit. According to the manufacturer's protocol, mitochondrial respiratory chain complex I and IV, and Mn-SOD levels in cells were assessed using the MEIMIAN Human Mitochondrial Respiratory Chain Complex I and IV ELISA kits (cat. nos. MM-60819H2 and MM-61261H2; Jiangsu ELISA Industry Co., Ltd.), and the Beyotime CuZn/Mn-SOD Activity Assay Kit (cat. no. S0103; Beyotime Institute of Biotechnology). OD values were measured at 450 nm using a full-wavelength microplate reader (Multiskan SkyHigh; Thermo Fisher Scientific, Inc.)

Malondialdehyde (MDA) detection. A total of $1x10^6$ cells were seeded in each well of 12-well plate and then proceeded with drug treatment. Adherent cells in 6-well plates were scraped and homogenized following the addition of an appropriate amount of Cell lysis buffer (cat. no. S0131S; Beyotime Institute of Biotechnology), the mixture was centrifuged (4˚C, 10,000 x g, 10 min) to obtain the supernatant. The protein concentration was measured using a BCA protein assay kit. To assess the content of MDA, an MDA detection kit was used (cat. no. S0131S; Beyotime Institute of Biotechnology) following the manufacturer's instructions. OD values were measured at 532 nm using a full-wavelength microplate reader (Multiskan SkyHigh; Thermo Fisher Scientific, Inc.).

ATP detection. A total of $1x10^6$ cells were seeded in each well of 6-well plate, then proceed with drug treatment. According to the manufacturer's instructions (cat. no. S0026; Beyotime Institute of Biotechnology), cells were lysed using an ATP detection lysis buffer and ATP content in the cells was extracted. The relative luminescence unit values were measured using a full-wavelength fluorescence microplate reader with a luminometric measurement module (Varioskan Flash; Thermo Fisher Scientific, Inc.).

Mitochondrial reactive oxygen species (mtROS) detection. MitoSOX Red (cat. no. M36005; Thermo Fisher Scientific, Inc.), a superoxide indicator, is a novel fluorescent probe that specifically targets and stains live cell mitochondria. Upon oxidation by mitochondrial superoxide, it generates bright red fluorescence. This assay was carried out following the manufacturer's instruction. Briefly, $1x10^6$ cells were seeded in each well of 12-well plate, the supernatant of the cell culture treated with drug was discarded after 24 h. A total of 1 ml of Hoechst 33342 live cell staining solution (5 μg/ml, 1:1,000) diluted in serum-free medium was added to each well and incubated at 37˚C in the dark for 15 min. Subsequently, the cells were washed three times with warm PBS and then treated with 2.5 μM MitoSOX Red diluted in serum-free medium, and incubated at 37˚C in the dark for 10 min; finally, the cells were washed three times with warm PBS. The fluorescence intensity of mtROS was observed and captured using an inverted fluorescence microscope (DMi8; Leica Biosystems) with an excitation wavelength of 396 nm and an emission wavelength of 610 nm.

Mitochondrial membrane potential (ΔΨm) detection. JC-1 is an ideal fluorescent probe used for detecting ΔΨm (24). When the ΔΨm is high, JC-1 aggregates in the mitochondrial matrix to form J-aggregates, producing red fluorescence; however, when the ΔΨm is low, JC-1 remains in a monomeric state and emits green fluorescence. According to the manufacturer's instructions (cat. no. C2003S; Beyotime Institute of Biotechnology), $1x10^4$ cells were seeded in a 12-well plate and treated with drugs. For the positive control group, carbonyl cyanide m-chlorophenyl hydrazone (10 mM, cat. no. C2003S-3; Beyotime Institute of Biotechnology) was added to the cell culture medium at a 1:1,000 dilution to achieve a final concentration of 10 μM. Cells were incubated in the dark at 37˚C for 20 min to abolish the membrane potential. Next, cells were incubated with prepared JC-1 working solution at 37˚C in the dark for 20 min. Cells were washed twice with JC-1 buffer solution and 500 μl serum-free culture medium was added, DAPI staining solution was then added at room temperature for 5 min. An inverted fluorescence microscope was used (DMi8; Leica Biosystems) to observe and capture images of JC-1 monomers under an excitation wavelength of 490 nm and an emission wavelength of 530 nm. Subsequently, images of JC-1 aggregates were captured under an excitation wavelength of 525 nm and an emission wavelength of 590 nm.

Structured illumination microscopy (SIM). A total of 10,000 cells were treated with BMS-202 (5 μM) labeled with Cy-3 for 24 h. After washing three times with warm PBS, PKMITO DEEP RED (250 μM) was diluted to a 1:2,500 ratio with preheated medium at 37˚C and incubated with the cells in the dark for 10 min. After washing three times with warm PBS, mitochondria were observed and captured using super-resolution SIM.

Scratch assay. Cells ($5x10^4$ cells) were seeded in each well of a 6-well plate and allowed to adhere until the cell coverage reached ≥80%. A sterile 200-μl pipette tip was then used to scratch a straight line in each well. Subsequently, the medium was removed and the cells were washed three times with PBS. For the control group, 2 ml complete DMEM was added, whereas for the experimental group, BMS-202 and GW were added separately and cultured for an additional 24 h during the assay. The plate was then placed under an inverted fluorescence microscope for image capture, and the area of the scratch was measured using ImageJ (version1 441, imagej.net/ij/features.html).

Tumor invasion assay. Cell invasion assay was performed using a 24-well Transwell chamber (8 μm, cat, 3422, Corning) coated with Matrigel (cat, 356234, Corning) at 37˚C for 2 h. A total of $1x10^5$ cells were dispersed in 200 μl serum-free culture medium and were seeded in the upper chamber. The lower chamber contained 800 μl DMEM supplemented with 10% FBS. For the experimental groups, 5 μM BMS-202 and 10 μM GW were added separately to the upper chambers, while the lower chambers remained unchanged. The cells were incubated at 37˚C for 24 h and the upper chamber was washed with PBS. Next, the Transwell insert was fixed in 4% paraformaldehyde at room temperature for 15 min, followed by another wash with PBS. The insert was then stained with hematoxylin solution at room temperature for 15 min. Finally, the insert was rinsed with PBS, placed under a light microscope for imaging and ImageJ was used to calculate the number of A375 cells invading through the insert.

Colony formation assay. A total of 200 cells were evenly seeded into each well of a 12-well culture plate. After cells adhered, they were treated with complete medium containing different drugs for 24 h. Following this, the medium was replaced with a drug-free complete medium. The medium was replaced every 3 days and cells were cultured for a total of 15 days. The colonies were fixed with 4% paraformaldehyde at room temperature for 15 min and stained with 1% crystal violet, both at room temperature for 15 min. The colonies (consisted of >50 cells) were quantified using ImageJ software (version 1.441).

Immunofluorescence analysis. For cell preparation, 10,000 cells were seeded at an confocal dishes. After the cells adhered, they were treated for 24 h. For fixation, cells were washed twice with PBS, fixed with 4% paraformaldehyde at room temperature for 15 min and then washed with PBS twice. For permeabilization, cells were treated with 0.1% Triton X-100 at room temperature for 10 min and then washed twice with PBS. For blocking, non-specific binding was blocked by incubating the cells with 5% BSA (cat. no. ST023; Beyotime Institute of Biotechnology) at room temperature for 1 h. The primary antibodies were diluted according to the manufacturer's instructions and added to the corresponding samples at 4˚C overnight, after which, the cells were washed three times with PBS. An Alexa Fluor® 561-conjugated secondary antibody (1:500, cat. no. A31572; Thermo Fisher Scientific, Inc.) was then used to incubate the cells at room temperature for 2 h, before being washed three times with PBS. DAPI staining solution was then added at room temperature for 5 min and the cells were washed three times with PBS. Finally, a fluorescence microscope (Leica Biosystems) was used for imaging followed by processing using ImageJ.

Flow cytometry. According to the manufacturer's instructions of the Annexin V-FITC Apoptosis Detection Kit (cat. no. C1062M; Beyotime Institute of Biotechnology), $1x10^6$ cells were seeded into 6-well plates and treated with drugs according to the experimental groups. After treatment, the cells were collected and stained with binding buffer containing PI and Annexin V-FITC for 15 min as per the protocol. Subsequently, the stained cells were analyzed by flow cytometry using BD FACSuite (version1.0.6, BD Biosciences,). BD FACS Aria III cell sorter (BD Biosciences).

Animals. A total of 20 4-week-old female BALB/c mice (average body weight, 15±0.5 g) were included in the present study. The BALB/c nude mice utilized in the present study were obtained from the Guangdong Provincial Medical Laboratory Animal Center and were subsequently housed in the Experimental Animal Center of Guangzhou Medical University (Guangzhou, China). The mice were maintained in 22-28˚C, humidity of 40-60%, and a 12-h light/dark cycle,

with free access to water and food. Female mice of specific pathogen-free grade were employed in all experimental procedures. The animal protocol was reviewed and approved by the Institutional Animal Care and Use Committee of The First Affiliated Hospital of Guangzhou Medical University (approval no. 20250034). All experimental procedures were conducted in strict accordance with the 3R principles (25) to ensure the humane treatment of animals.

In vivo treatments. Mice were randomly divided into the following four groups (n=5/group): Ctrl, BMS-202 20 mg/kg, GW 10 mg/kg, and BMS-202 20 mg/kg + GW 10 mg/kg. The mice initially received a subcutaneous injection of 100 μl culture medium containing 5x10^6 A375 cells into the dorsal region. When the tumor size reached 50-100 mm^3 (length x $width^2$/2), therapeutic treatments were initiated according to the experimental groups via intraperitoneal injection: BMS-202 (20 mg/kg), GW (10 mg/kg) or an equivalent volume of saline for the control group. Treatments were administered every 3 days. Mouse body weight was monitored using a microbalance every 3 days, and tumor size was measured with calipers every 3 days. The maximum tumor volume was set as 1,500 mm^3. On the third day after the third drug injection, mice were anesthetized with 5% isoflurane and were euthanized by cervical dislocation. Death was confirmed by observing the cessation of breathing and heartbeat.

H&E staining and immunohistochemistry. Following euthanasia, tumor tissue was harvested from the dorsal region of tumor-bearing mice. Tumor samples were fixed overnight in 4% paraformaldehyde at 4˚C and subsequently embedded in paraffin. Sections (5 μm) were prepared and dewaxed, followed by antigen retrieval using citrate buffer at 98˚C for 5 min and permeabilized with 0.1% Triton X-100. Endogenous enzymatic activity was quenched with 3% H_2O_2 at room temperature for 20 min. Blocking was performed with 10% goat serum (cat. no. PN0038; Pinuofei Biological) at 37˚C for 30 min. Sections were then incubated with primary antibodies specific to modified Ki67 (1:500, cat. no. ABB00008; Shanghai Huilan Biotechnology Co., Ltd.) at 4˚C overnight. Subsequently, sections were incubated with biotinylated secondary antibody (1:500, Peroxidase-Labeled, cat, 5220-0336, SeraCare Life Sciences) at room temperature for 1 h, followed by incubation with the DAB complex (cat, DAB-4033, Fuzhou Maixin Biotechnology Co., Ltd.) at room temperature for 5 min. Target protein expression was visualized using DAB substrate. H&E was performed at room temperature for 5 min. Image acquisition was performed using a light microscope(PANNORAMIC SCAN; 3DHISTECH).

Statistical analysis. Each experiment was repeated at least 3 times. The experimental results were analyzed using GraphPad Prism (version 9.0; Dotmatics). The significance of differences between two groups was determined using an unpaired Student's t-test. For comparisons between >2 groups, one-way ANOVA was performed, followed by Tukey's test. All data are presented as the mean ± standard deviation. $P<0.05$ was considered to indicate a statistically significant difference.

Results

BMS-202 inhibits tumor cell function and promotes apoptosis. BMS-202 (Fig. 1A) is a small molecule PD-L1 inhibitor that exerts its effects by directly binding to PD-L1 and blocking the interaction between human PD-1 and PD-L1. In the present study, western blotting revealed that BMS-202 reduced the expression levels of PD-L1 in A375 cells (Fig. 1C). Subsequently, a cell viability assay was carried out to determine the IC_{50} of BMS-202; for subsequent experiments, a concentration of 5 μM and a treatment time of 24 h. BMS-202 inhibited cell viability (Fig. 1B). Analysis of tumor cell functions, including migration and invasion revealed that BMS-202 significantly reduced both (Fig. 1D and E). Furthermore, RT-qPCR analysis revealed an increase in the mRNA expression levels of the pro-apoptotic factor Bax and a decrease in the mRNA expression levels of the anti-apoptotic factor Bcl-2 (Fig. 1F), suggesting that BMS-202 promotes apoptosis. This finding was further confirmed by western blotting, which showed similar results at the protein level (Fig. 1G). These data collectively indicated that BMS-202 may inhibit tumor cell functions and promote apoptosis.

BMS-202 enhances mitochondrial function. MT-CO1, MT-CO3 and MT-ND4 are mitochondrial genes that encode key proteins of the mitochondrial respiratory chain, which participate in the functions of the cytochrome *c* oxidase complex and the NADH dehydrogenase (ND) complex during cellular respiration (26). They are essential for maintaining mitochondrial energy metabolism and ATP production. The present study revealed that BMS-202 increased the expression levels of the mitochondrial genes MT-CO1 and MT-ND4, whereas no significant change was observed in MT-CO3 expression levels (Fig. 2A). Further analysis of the mitochondrial respiratory chain complex expression revealed an upregulation of complexes I and IV (Fig. 2B), along with a significant increase in ATP levels (Fig. 2C). These results suggested that BMS-202 may enhance mitochondrial function by promoting the expression of key respiratory chain complexes and boosting ATP production.

BMS-202 enters the mitochondria and binds to PD-L1. To identify the effects of BMS-202 on tumor cells, the impact of BMS-202 on mitochondrial function was investigated by labelling the compound with Cy-3. First, A375 cells were incubated with 5 μM BMS-202-Cy-3 for 24 h. Using low magnification (magnification, x10), it was observed that BMS-202 entered the cells (Fig. 3A). To further investigate the intracellular dynamics, live-cell imaging was carried out using SIM at high magnification (x100), which revealed that BMS-202 was localized to the mitochondria (Fig. 3B). To confirm the binding of BMS-202 to mitochondrial PD-L1, samples were fixed and immunofluorescence was carried out. Analysis revealed that BMS-202 specifically bound to PD-L1 within the mitochondria (Fig. 3C). Furthermore, Mitochondrial proteins were extracted and PD-L1 expression was assessed by western blotting but failed to detect PD-L1 in mitochondrial isolates, likely due to its low abundance below detection limits (data not shown). Notably, the relationship between increased apoptosis and tumor activity inhibition caused by BMS-202, and its concurrent enhancement of mitochondrial function remains unclear.

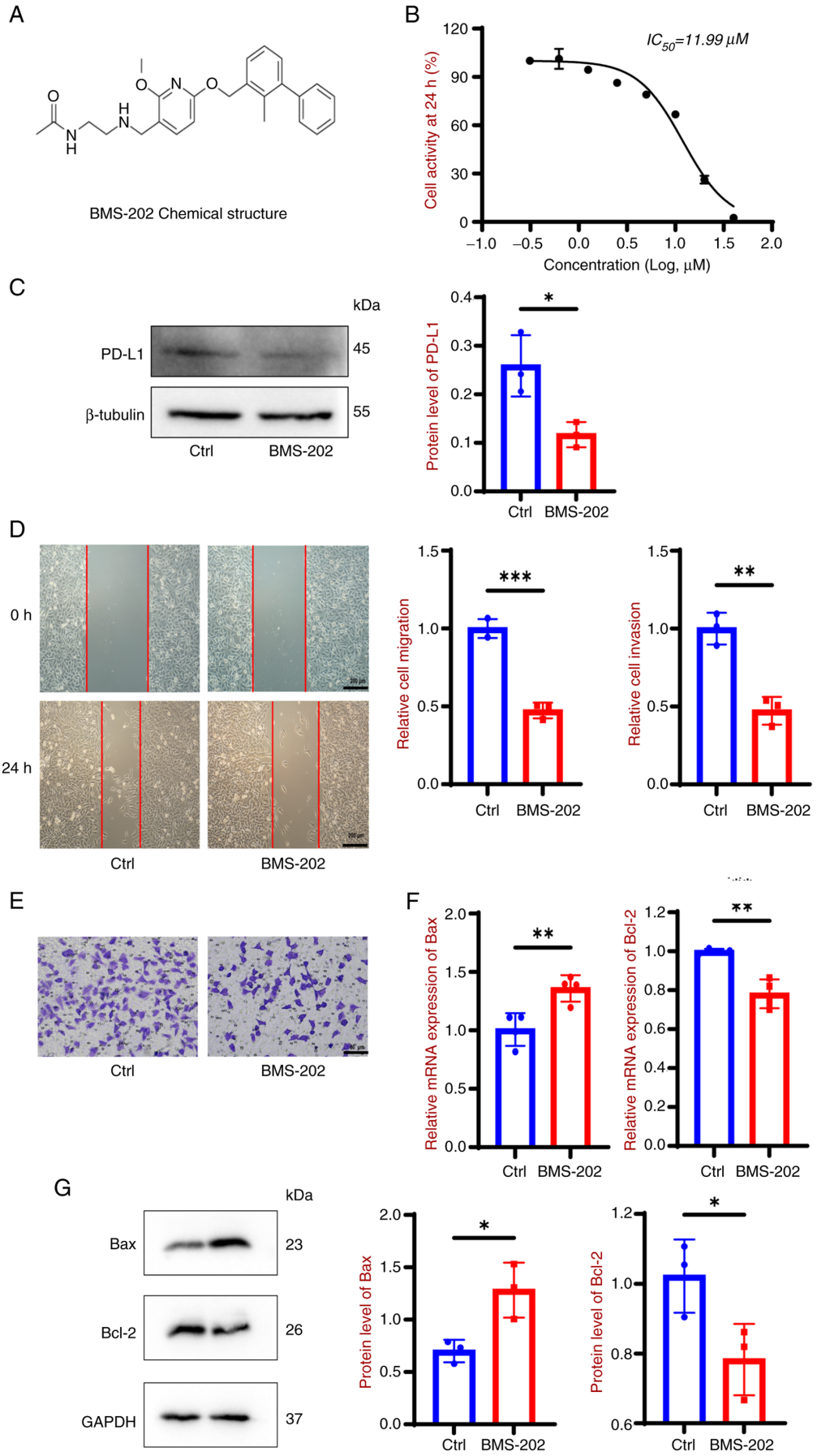

Figure 1. BMS-202 inhibits A375 cell viability, migration and invasion, and induces apoptosis. (A) Chemical structure of BMS-202. (B) Cell Counting Kit-8 assay of cell viability and determine the IC_{50} of BMS-202. (C) Assessment of PD-L1 expression by western blotting. (D) Assessment of cell migration. (E) Evaluation of cell invasion. (F) Reverse transcription-quantitative PCR of mRNA expression levels of the pro-apoptotic protein Bax and the anti-apoptotic protein Bcl-2. (G) Western blotting of the protein expression levels of Bax and Bcl-2. *P<0.05, **P<0.01, ***P<0.001. Ctrl, control.

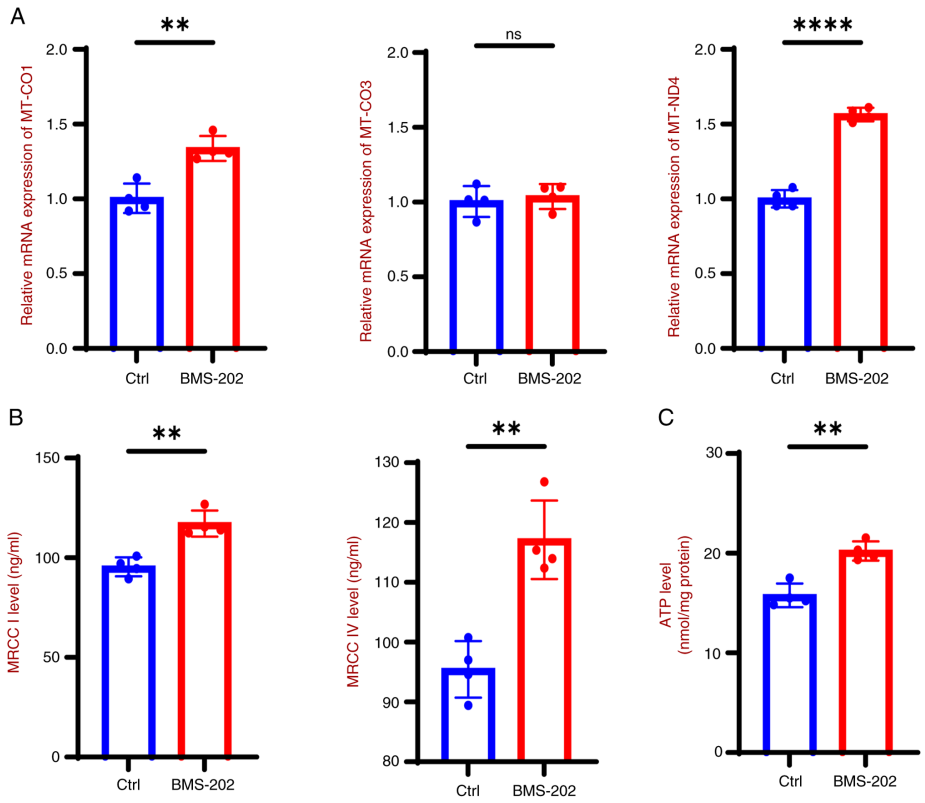

Figure 2. BMS-202 enhances mitochondrial respiratory chain complex expression levels and increases ATP levels. (A) Reverse transcription-quantitative PCR analysis of the mRNA expression levels of MT-CO1, MT-CO3 and MT-ND4. (B) ELISA of MRCC I and IV levels. (C) ATP quantification assay. ns, no significant difference; **P<0.01, ****P<0.0001. Ctrl, control; MT-CO, mitochondrially encoded cytochrome *c* oxidase; MT-ND4, mitochondrially encoded NADH dehydrogenase 4; MRCC, Mitochondrial respiratory chain complex.

GW inhibits BMS-202-induced enhancement of mitochondrial function. To further investigate the surprising impact of BMS-202 on mitochondrial function, the pyruvate carrier inhibitor GW was used to block these effects on mitochondria. First, cell viability was assessed using the CCK-8 assay and the IC_{50} of GW was determined (Fig. 4A), based on the result of IC_{50}, 10 μM was selected as the experimental concentration. Analysis revealed that GW effectively inhibited the BMS-202-induced increase in MT-CO1, MT-ND4 and MT-ND5 (another core part of ND complex I), mRNA levels (Fig. 4B); this finding was confirmed by western blotting (Fig. 4C). Additionally, ELISA demonstrated that GW successfully reduced the levels of mitochondrial respiratory chain complex I and IV (Fig. 4D), and ATP (Fig. 4E). The results indicated that GW effectively attenuated the increase in mitochondrial respiratory chain function induced by BMS-202. To comprehensively evaluate the changes in mitochondrial function, the ΔΨm was further assessed, revealing that BMS-202 increased the ΔΨm in A375 cells, whereas GW inhibited this increase (Fig. 4F). In conclusion, GW effectively suppressed the mitochondrial function enhancement induced by BMS-202.

GW inhibits the reduction of mitochondrial oxidative stress induced by BMS-202. Given the close relationship between mitochondria and oxidative stress, the effects of BMS-202 on oxidative stress were investigated further. Compared with the control group, BMS-202 effectively reduced intracellular MDA levels (Fig. 5B) and increased Mn-SOD activity in mitochondria (Fig. 5A). while GW exhibited the opposite effects. Notably, BMS-202 reduced the elevated Mt-ROS levels induced by GW (Fig. 5C), indicating its role in stabilizing intracellular ROS levels. These findings suggested that BMS-202 may alleviate oxidative stress.

GW promotes apoptosis induced by BMS-202. To investigate the relationship between increased mitochondrial function and apoptosis, the effect of combined GW and BMS-202 treatment on apoptosis was examined. Bax, caspase-3, caspase-8 and PARP are well-known pro-apoptotic factors, whereas Bcl-2 is a common anti-apoptotic factor (27). RT-qPCR revealed that the combination of GW and BMS-202 significantly upregulated Bax expression, whereas it downregulated Bcl-2 expression compared with BMS-202 (Fig. 6A). This was corroborated by western blotting results (Fig. 6B), where the expression and activation of caspase-3 and PARP were specifically assessed to evaluate apoptosis levels. GW and BMS-202 increased expression of cleaved caspase-3 and cleaved PARP compared to the BMS-202 (Fig. 6B). Additionally, cell immunofluorescence assays indicated that the BMS-202+GW group exhibited stronger caspase-3 and caspase-8 fluorescence intensity compared to the BMS-202 group (Fig. 6C). Furthermore, flow cytometry was carried out to assess apoptosis and confirmed GW can promote apoptosis induced by BMS-202 (Fig. 6D). These findings suggested that the inhibition of BMS-202-induced mitochondrial function enhancement further promotes apoptosis. The use of GW alone also promoted apoptosis, suggesting that short-term inhibition of mitochondrial respiration can enhance apoptotic processes.

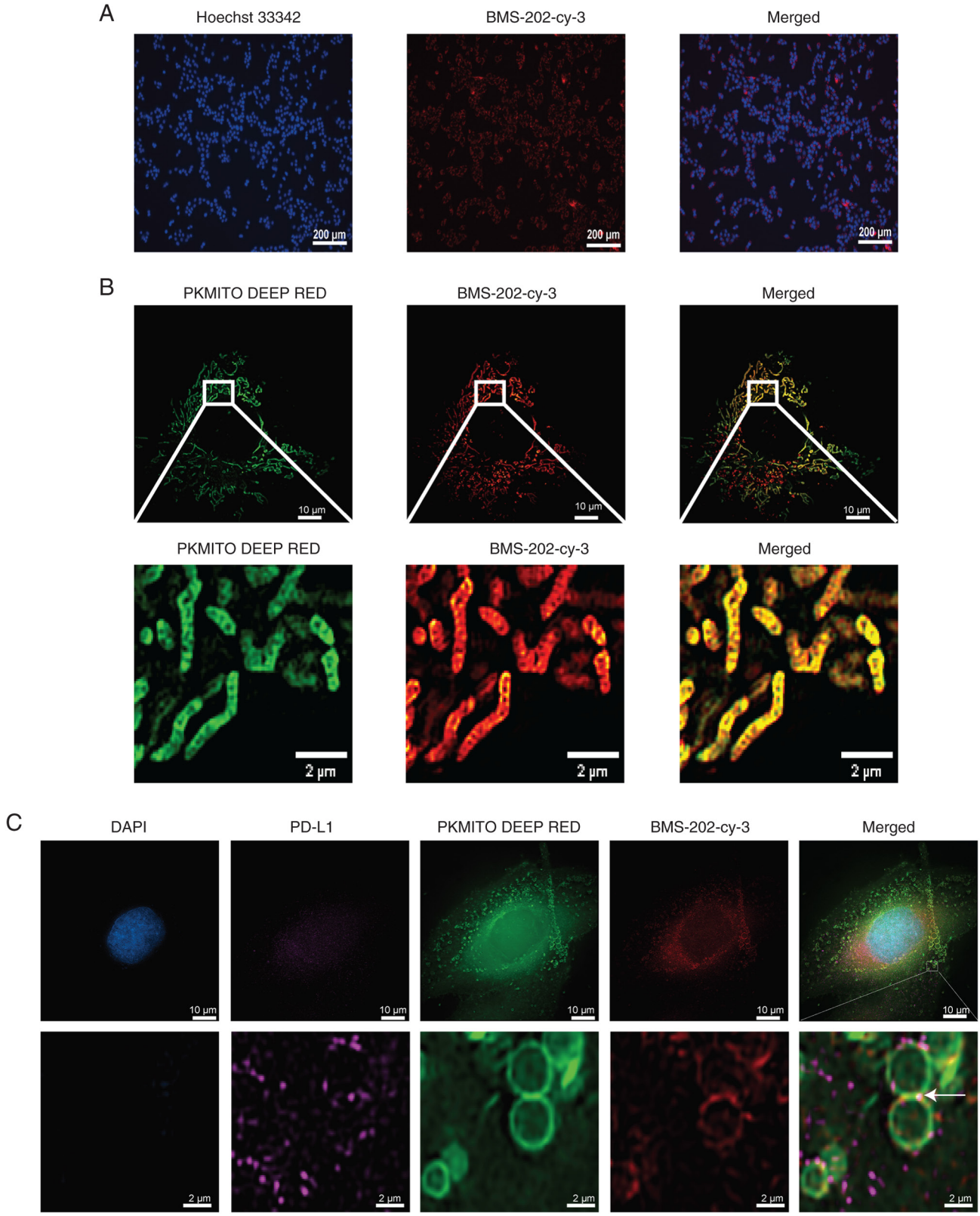

Figure 3. Localization of BMS-202 in cells. (A) BMS-202 localization within cells observed under low magnification (magnification, x10). (B) Live-cell imaging using structured illumination microscopy to examine the mitochondrial localization of BMS-202 (magnification, x100). (C) Immunofluorescence analysis showing the binding of BMS-202 to PD-L1 (magnification, x100). PD-L1, programmed cell death ligand 1.

GW enhances the reduction of tumor function induced by BMS-202. To further investigate the role of the mitochondrial pathway in the tumor cell function changes induced by BMS-202, the combined effects of GW and BMS-202 on tumor proliferation, migration and invasion were examined. Analysis revealed that GW significantly enhanced the inhibitory effects of BMS-202 on tumor cell proliferation (Fig. 7A), migration (Fig. 7B) and invasion (Fig. 7C). Moreover, GW

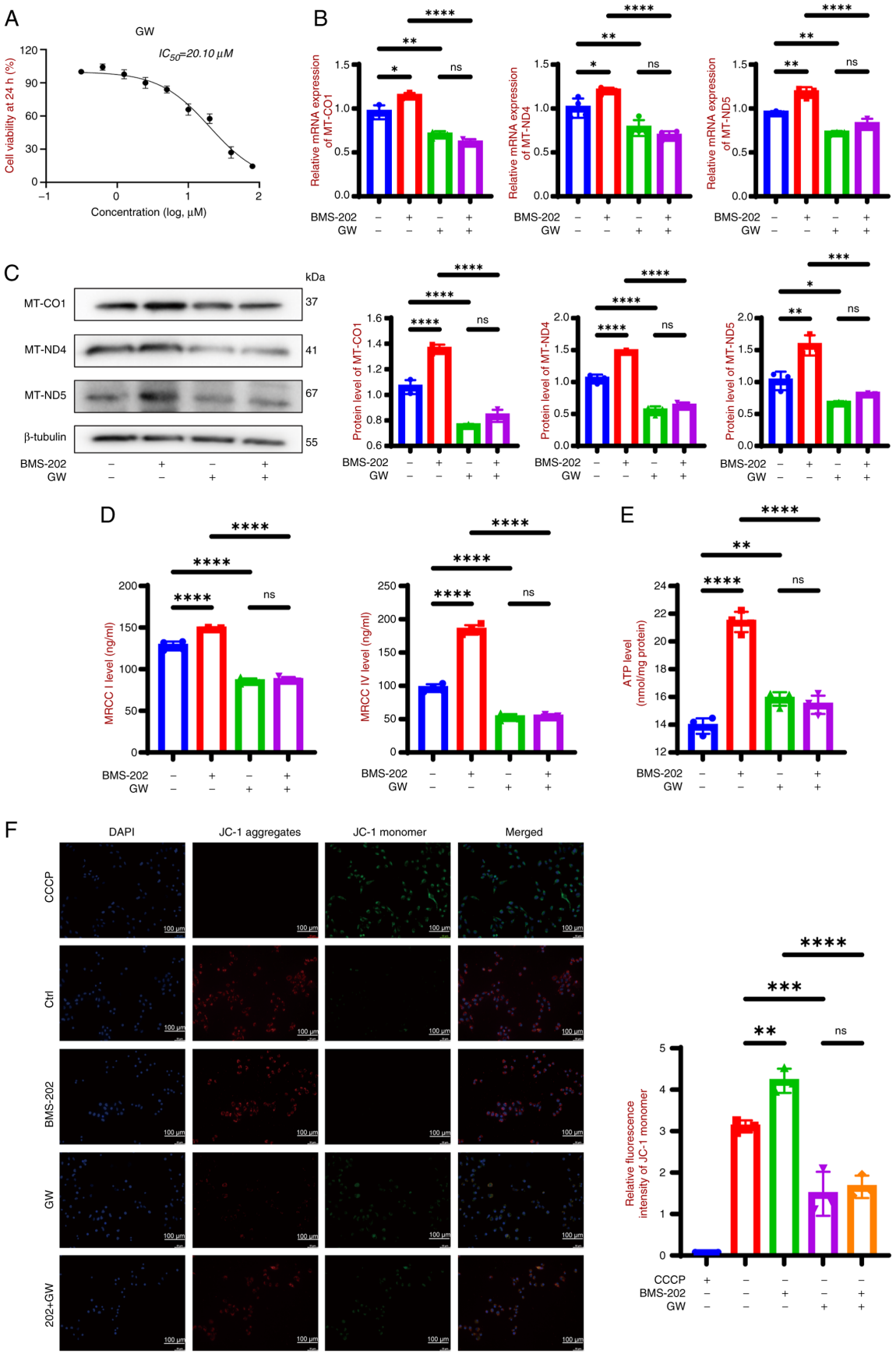

Figure 4. Effect of GW on the enhancement of mitochondrial function induced by BMS-202. (A) Determination of the IC_{50} of GW. (B) Reverse transcription-quantitative PCR analysis of the mRNA expression levels of MT-CO1, MT-ND4 and MT-ND5. (C) Western blotting was performed to assess the protein expression levels of MT-CO1, MT-ND4 and MT-ND5. (D) ELISA measurement of MRCC I and IV levels. (E) ATP level quantification. (F) JC-1 fluorescence assay was performed to evaluate mitochondrial membrane potential. ns, no significant difference; *P<0.05, **P<0.01, ***P<0.001, ****P<0.0001. CCCP, carbonyl cyanide m-chlorophenyl hydrazone; Ctrl, control; MT-CO, mitochondrially encoded cytochrome c oxidase; MT-ND, mitochondrially encoded NADH dehydrogenase; GW, GW604714X; MRCC, Mitochondrial Respiratory Chain Complex.

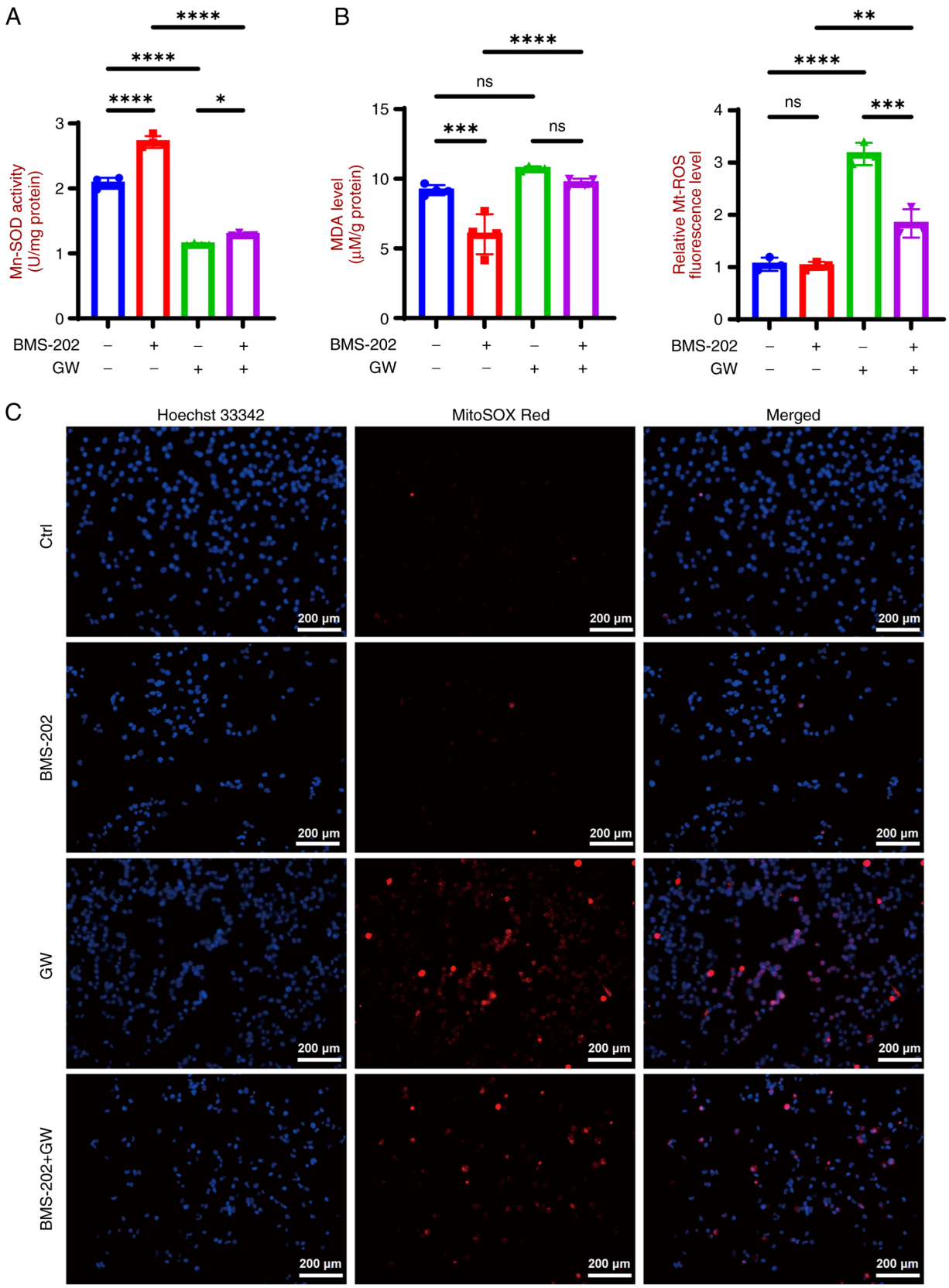

Figure 5. GW inhibits changes in oxidative stress levels induced by BMS-202. (A) Detection of Mn-SOD activity in mitochondria. (B) Detection of MDA levels. (C) Detection of Mt-ROS. ns, no significant difference; *P<0.05, **P<0.01, ***P<0.001, ****P<0.0001. SOD, superoxide dismutase; MDA, malondialdehyde; Mt-ROS, mitochondrial reactive oxygen species. GW, GW604714X.

treatment notably reduced colony formation induced by BMS-202(Fig. 7D). These findings suggested that targeting the mitochondrial pathway may amplify the direct antitumor effects of BMS-202.

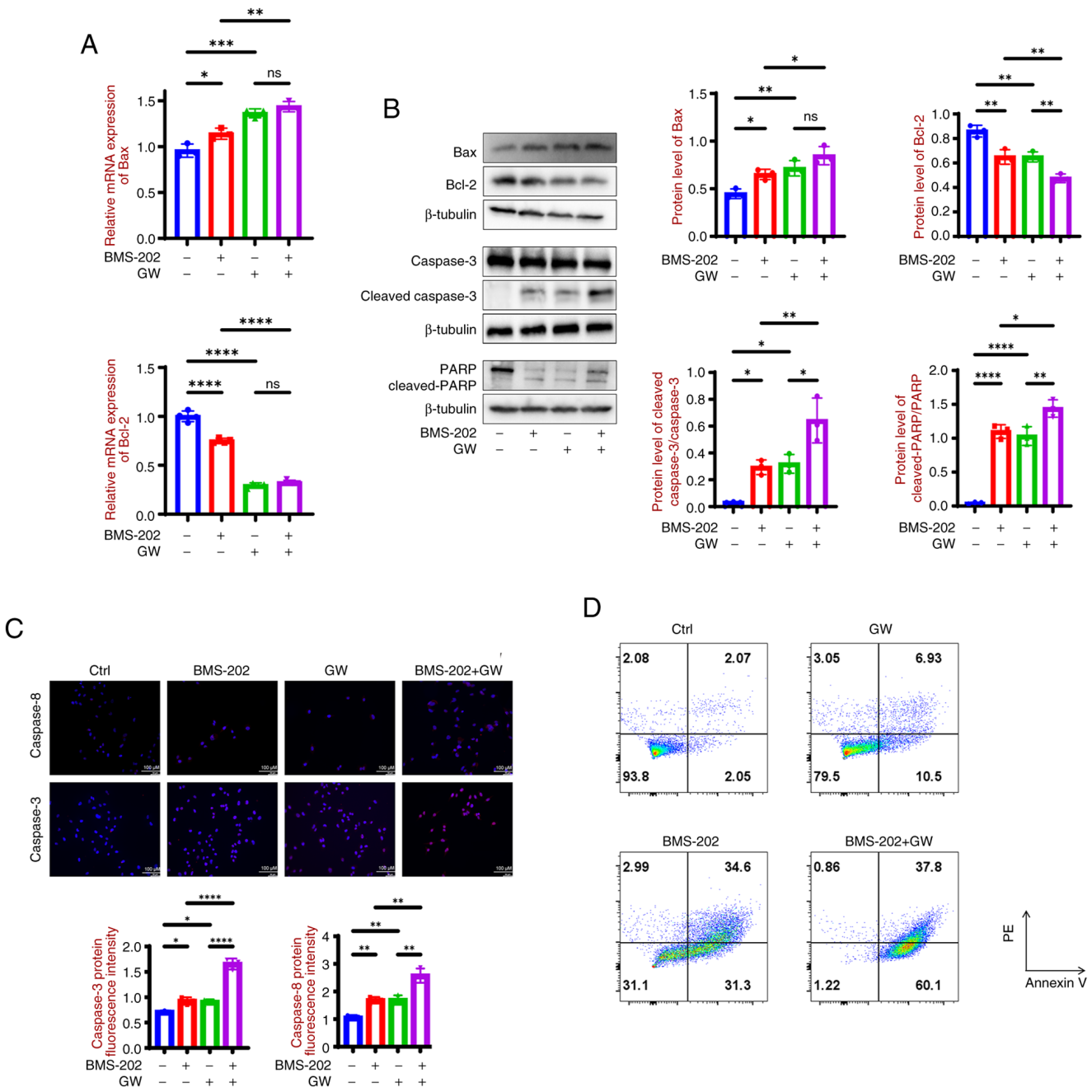

Figure 6. Assessment of apoptosis levels. (A) Changes in Bcl-2 and Bax mRNA expression levels were detected by reverse transcription-quantitative PCR. (B) Changes in Bax, Bcl-2, cleaved-caspase-3 and cleaved-PARP protein expression were detected by western blotting. (C) Analysis of caspase-3 and caspase-8 expression by cellular immunofluorescence. (D) Flow cytometric analysis of cell apoptosis. *P<0.05, **P<0.01, ***P<0.001, ****P<0.000. Ctrl, control; PARP, poly(ADP-ribose) polymerase.

Animal experiments verify that GW can enhance the inhibition of tumor proliferation induced by BMS-202. To validate the antitumor effects, xenograft tumors were established in nude mice and the drugs were administered via intraperitoneal injection. The detailed experimental workflow is shown in Fig. 8A and Tumor-bearing mice is shown in Fig. 8B. Tumor proliferation was evaluated by measuring tumor size and volume. The results revealed that GW significantly enhanced the inhibitory effect of BMS-202 on tumor proliferation (Fig. 8C and E), while no significant changes were observed in mouse body weight (Fig. 8D). Ki-67, a nuclear protein associated with cell cycle progression, serves as a biomarker indicative of the proportion of cells in active proliferation. Tumor specimens collected from the subcutaneous tissues of tumor-bearing mice were sectioned and subjected to both H&E staining and Ki-67 immunohistochemical analysis. H&E results revealed that after the combination treatment with BMS-202 and GM, the cell density in the tumor tissue was markedly reduced, the cellular atypia was alleviated, the pathological mitosis decreased and the vascular distribution was improved (Fig. 8F). The Ki-67-positive cell rate was significantly reduced by BMS-202 treatment compared to the control group, whereas the Ki-67 positivity ratio was further decreased by coadministration with GW (Fig. 8G).

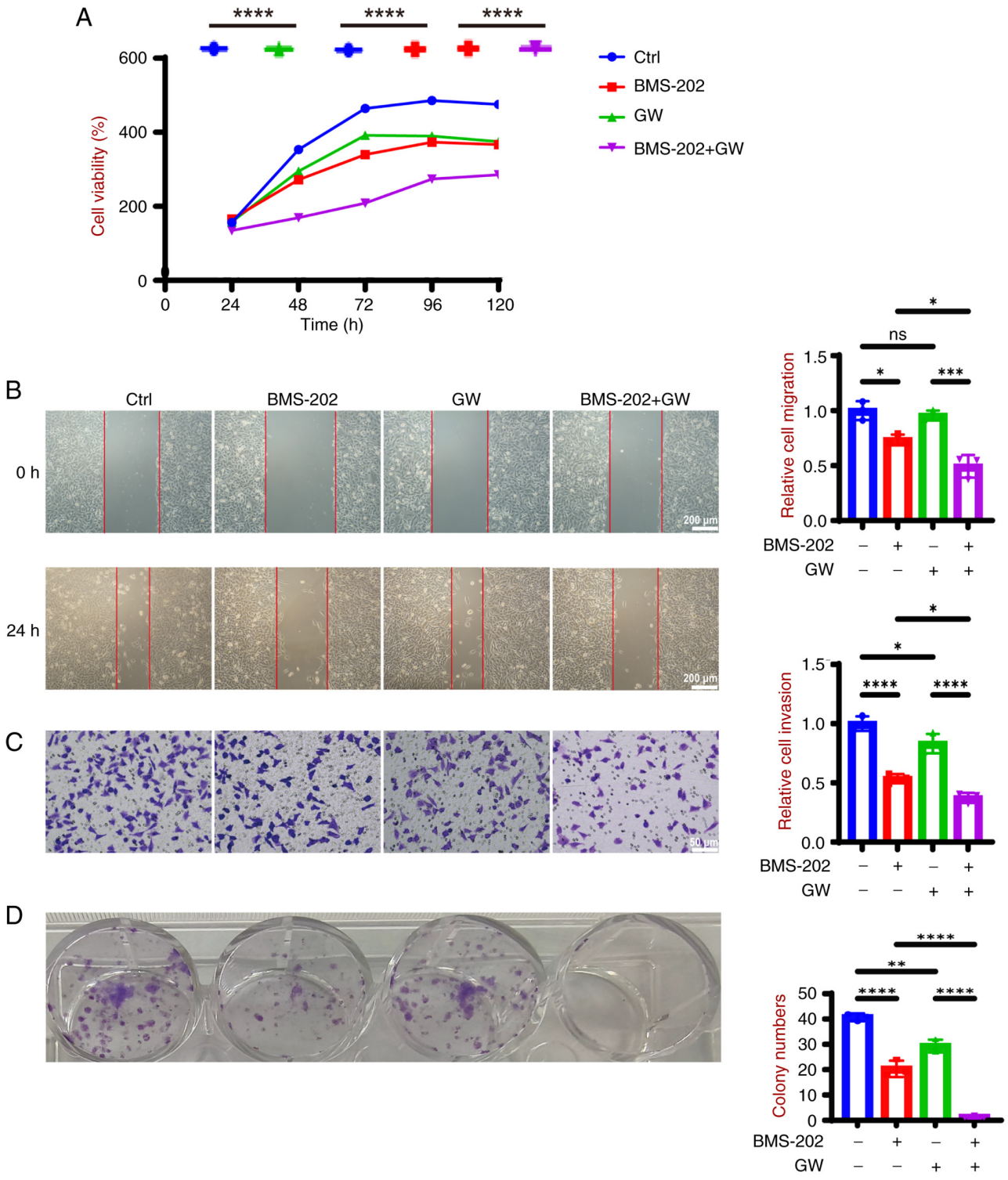

Figure 7. Changes in tumor cell function. (A) Cell Counting Kit-8 assay was used to assess changes in cell viability. (B) Cell migration assay was performed to assess changes in migration. (C) Cell invasion assay was performed to assess changes in invasion. (D) Clonogenic assay was used to detect cell proliferation ability. ns, no significant difference; *P<0.05, **P<0.01, ***P<0.001, ****P<0.0001. GW, GW604714X.

Collectively, the *in vivo* experiments corroborated the findings from the *in vitro* experiments, demonstrating consistent antitumor effects.

Discussion

MM remains a notable therapeutic challenge, particularly at advanced stages where resistance to conventional therapies is common (8). Notably, immune checkpoint inhibitors targeting the PD-1/PD-L1 axis have revolutionized melanoma treatment and their mechanisms are traditionally attributed to restoring T cell-mediated immunity (28). PD-L1 inhibitors may also directly impair the metabolic pathways of tumor cells (11,14) yet this remains underexplored.

In the present study, it was shown that the small-molecule PD-L1 inhibitor BMS-202 exerted direct antitumor effects

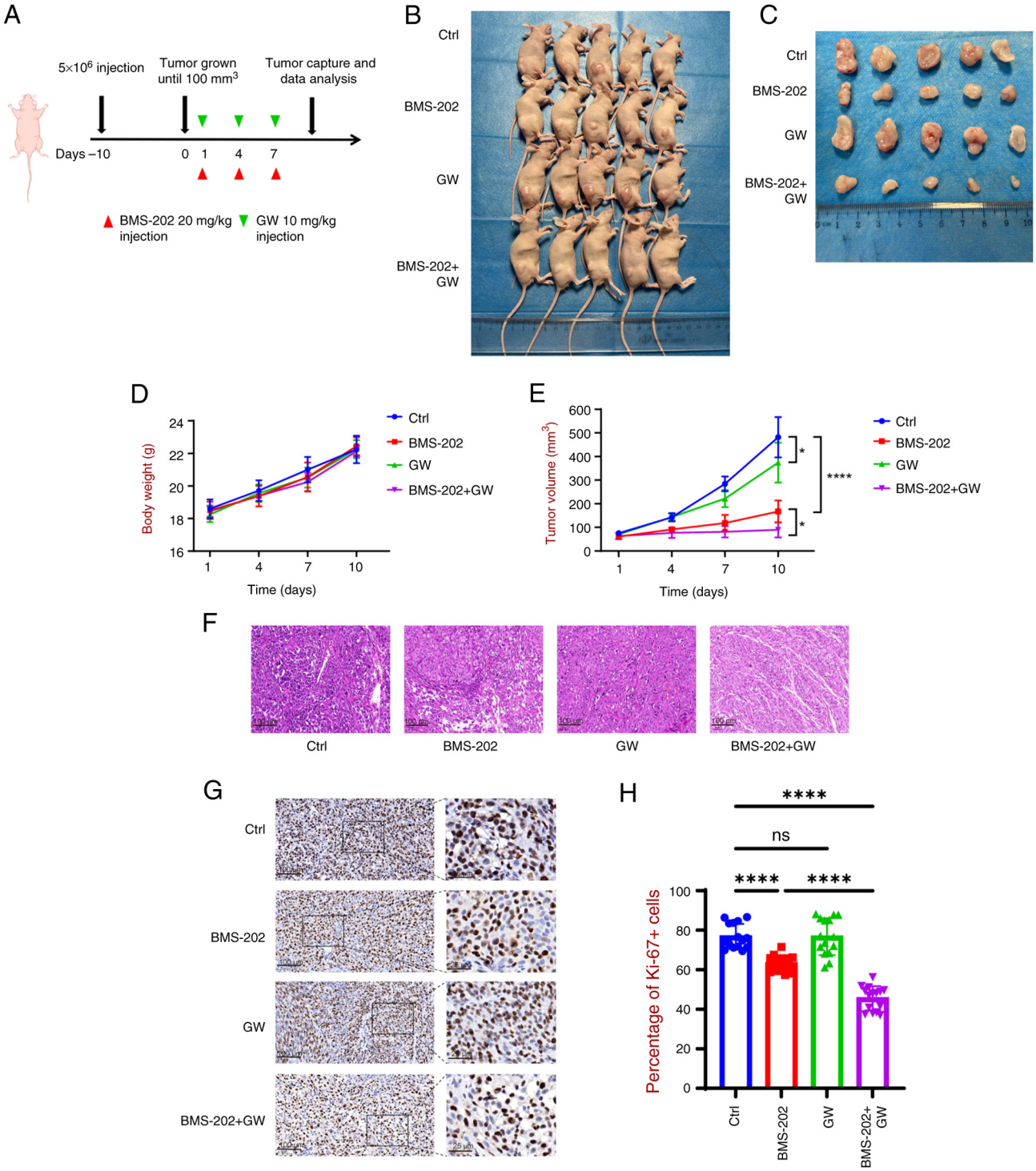

Figure 8. Evaluation of tumor proliferation *in vivo*. (A) Animal experimental procedure. (B) Tumor-bearing mice. (C) Comparison of tumor sizes. (D) Weight changes in tumor-bearing mice. (E) Comparison of tumor volume (F) H&E staining (magnification, 20x). (G) Tumor proliferation was assessed by immunohistochemical analysis of Ki-67 (magnification, 20x). (H) Fluorescence intensity of Ki-67. ns, no significant difference; ****P<0.05; ****P<0.0001. Ctrl, control. GW, GW604714X.

on A375 melanoma cells. BMS-202 penetrates melanoma cells and localizes to the mitochondria, where it binds to mitochondrial PD-L1. This interaction enhances mitochondrial respiratory complex activity and ATP production, yet it promotes apoptosis. Apoptosis is principally mediated through two evolutionarily conserved pathways: The extrinsic pathway initiated by death receptor activation and the intrinsic pathway regulated by mitochondrial permeability transition. Both pathways converge on caspase cascades that execute programmed cell death (27). While BMS-202 was shown to enhance mitochondrial respiration, it simultaneously disrupted tumor cell proliferation and promoted apoptosis. This apparent paradox may be attributed to the compartmentalized distribution of PD-L1 within cellular subdomains (29) potentially having distinct functions. The pro-apoptotic effects of BMS-202 may be mediated through

mechanisms distinct from its mitochondrial bioenergetic modulation. While Xie *et al* (12) proposed that mitochondrial PD-L1 may interfere with pro-survival signaling pathways or mitophagy, the present study suggested that mitochondrial PD-L1 may serve as a metabolic checkpoint, balancing energy production and survival signals. While the precise mechanism linking enhanced mitochondrial function to apoptosis remains unclear, the present study highlights a dual role for BMS-202; it disrupts PD-L1-mediated immune evasion while also directly reprogramming tumor cell metabolism to favor death over survival.

Xie *et al* (12) suggested that PD-L1 is present in mitochondria; however, there is currently no evidence that PD-L1 inhibitors can penetrate these organelles. Therefore, whether PD-L1 inhibitors can access mitochondria remains uncertain. Imaging live-cell mitochondria is vital for understanding their role, and SIM has been shown to be particularly effective in this context (30-32). The present study employed ultra-high-resolution SIM to investigate A375 melanoma cells. It was revealed that BMS-202 could enter the mitochondria of these cells and bind to PD-L1; however, it was not possible to identify a method to prevent BMS-202 from entering mitochondria, making it challenging to establish a direct connection between its entry and enhanced mitochondrial function. This finding suggested that the PD-1/PD-L1 pathway may have implications beyond immune evasion, potentially influencing mitochondrial function as well. The present study therefore focused on exploring the specific effects and mechanisms of this interaction.

Mitochondria carry out a key role in cancer and immunotherapy, and their significance has been widely studied (18,33,34). Beyond generating ATP for energy, mitochondria are involved in tumor metabolism, redox balance, calcium homeostasis, transcriptional regulation and programmed cell death (35-37). An increase in OXPHOS could enhance ATP levels, which supports tumor cell survival and provides the energy needed for tumor progression (13,34). Moreover, enhanced mitochondrial function may suppress glycolysis, reducing the production of other biomolecules, such as nucleotides, amino acids and lipids (38), thus hindering the rapid proliferation of tumor cells. These changes in mitochondrial function could also impact the effectiveness of PD-1/PD-L1 therapies (13). The present study revealed that BMS-202 could significantly enhance mitochondrial function. Specifically, it increased the expression of mitochondrial respiratory chain complexes I and IV, and enhanced ATP production, thereby supplying more energy for tumor activity. This boost in energy supply may support tumor activity. Additionally, BMS-202 reduced the high levels of mitochondrial ROS caused by GW, thereby mitigating mitochondrial oxidative stress. The imbalance of ROS is a key factor in cancer progression, and theoretically, lowering ROS levels can promote cell survival (39-41). This may contribute to the frequent occurrence of resistance observed in response to PD-1/PD-L1 therapies.

To investigate the impact of enhanced mitochondrial function on tumor cells, the pyruvate carrier inhibitor GW was used to suppress mitochondrial activity. The data revealed that the combination of BMS-202 and GW significantly inhibited cell proliferation, reduced the migratory capacity of tumor cells and further promoted apoptosis. Notably, our present study demonstrated that GW could reduce the levels of OXPHOS and promote apoptosis, but it failed to decrease ATP levels in A375 cells. It may be hypothesized that this is due to the Warburg effect in tumor cells, where the inhibition of mitochondrial respiration leads to enhanced anaerobic glycolysis (42,43). In summary, the present study demonstrated that BMS-202 has a direct antitumor effect at the cellular level, while enhancing mitochondrial function. By using GW to disrupt the mitochondrial regulatory effects of BMS-202, its antitumor impact was further amplified. This highlights the importance of understanding the interaction between mitochondrial activity and immunotherapy, as it may provide new strategies to improve treatment outcomes.

The results of the present study have demonstrated that PD-L1 in the mitochondria can modulate mitochondrial function and is associated with cell viability. However, the precise role and underlying mechanisms of PD-L1 within the mitochondria have not yet been fully elucidated. Systematic analyses of mitochondrial PD-L1 biology represent a key frontier for future investigation. Targeting these pathways could potentially overcome resistance to PD-L1 inhibitors, optimizing therapeutic efficacy. In conclusion, the present study highlighted the direct effects of BMS-202 on A375 cells. This approach could pave the way for more effective treatments for melanoma.

Acknowledgements

Not applicable.

Funding

The present study was supported by the National Natural Science Foundation of China (grant no. 82074172), the Natural Science Foundation of Guangdong Province, China (grant no. 02820005), Guangzhou City's Construction Project for Tier-Three Famous Traditional Chinese Medicine Clinics (grant no. 3208203801) and the Zhongnanshan Medical Foundation of Guangdong Province (grant no. ZNSA-2020013).

Availability of data and materials

The data generated in the present study can be requested from the corresponding author.

Authors' contributions

XC, ZL, NZ, YW contributed to the study conception and design. NZ, FF, RD, XZ, XW, YY, JD, YW, ZW, WM, XH, SZ, YD, CH performed experiments. XC, ZL, NZ, FF, CF, PY conducted data analysis and interpretation. XC, ZN, FFL, ZL wrote and revised the manuscript. XC, ZL acquired the financial support for the project. All authors read and approved the final manuscript. NZ and FL confirm the authenticity of all the raw data.

Ethics approval and consent to participate

The animal protocol was reviewed and approved by the Institutional Animal Care and Use Committee of The

First Affiliated Hospital of Guangzhou Medical University (approval no. 20250034).

Patient consent for publication

Not applicable.

Competing interests

The authors declare that they have no competing interests.

Use of artificial intelligence tools

During the preparation of this work, AI tools (ChatGPT4.0) were used to improve the readability and language of the manuscript, and subsequently, the authors revised and edited the content produced by the AI tools as necessary, taking full responsibility for the ultimate content of the present manuscript.

References

1. Iacono D, Vitale MG, Basile D, Pelizzari G, Cinausero M, Poletto E, Pascoletti G and Minisini AM: Immunotherapy for older patients with melanoma: From darkness to light? Pigment Cell Melanoma Res 34: 550-563, 2021.
2. Tímár J and Ladányi A: Molecular pathology of skin melanoma: Epidemiology, differential diagnostics, prognosis and therapy prediction. Int J Mol Sci 23: 5384, 2022.
3. Mallardo D, Basile D and Vitale MG: Advances in melanoma and skin cancers. Int J Mol Sci 26: 1849, 2025.
4. Sinikumpu SP, Jokelainen J, Keinänen-Kiukaanniemi S and Huilaja L: Skin cancers and their risk factors in older persons: A population-based study. BMC Geriatr 22: 269, 2022.
5. Keung EZ and Gershenwald JE: The eighth edition American Joint Committee on Cancer (AJCC) melanoma staging system: Implications for melanoma treatment and care. Expert Rev Anticancer Ther 18: 775-784, 2018.
6. Wild CP, Weiderpass E and Stewart BW: World Cancer Report: Cancer Research for Cancer Prevention. IARC Publications, Lyon, 2020.
7. Wang Y, Gu T, Tian X, Li W, Zhao R, Yang W, Gao Q, Li T, Shim JH, Zhang C, *et al*: A small molecule antagonist of PD-1/PD-L1 interactions acts as an immune checkpoint inhibitor for NSCLC and melanoma immunotherapy. Front Immunol 12: 654463, 2021.
8. Long GV, Swetter SM, Menzies AM, Gershenwald JE and Scolyer RA: Cutaneous melanoma. Lancet 402: 485-502, 2023.
9. Andrews LP, Butler SC, Cui J, Cillo AR, Cardello C, Liu C, Brunazzi EA, Baessler A, Xie B, Kunning SR, *et al*: LAG-3 and PD-1 synergize on CD8+ T cells to drive T cell exhaustion and hinder autocrine IFN-γ-dependent anti-tumor immunity. Cell 187: 4355-4372.e22, 2024.
10. Geels SN, Moshensky A, Sousa RS, Murat C, Bustos MA, Walker BL, Singh R, Harbour SN, Gutierrez G, Hwang M, *et al*: Interruption of the intratumor CD8+ T cell: Treg crosstalk improves the efficacy of PD-1 immunotherapy. Cancer Cell 42: 1051-1066.e7, 2024.
11. Yang X, Wang W and Ji T: Metabolic remodeling by the PD-L1 inhibitor BMS-202 significantly inhibits cell malignancy in human glioblastoma. Cell Death Dis 15: 186, 2024.
12. Xie XQ, Yang Y, Wang Q, Liu HF, Fang XY, Li CL, Jiang YZ, Wang S, Zhao HY, Miao JY, *et al*: Targeting ATAD3A-PINK1-mitophagy axis overcomes chemoimmunotherapy resistance by redirecting PD-L1 to mitochondria. Cell Res 33: 215-228, 2023.
13. Du F, Yang L, Liu J, Wang J, Fan L, Duangmano S, Liu H, Liu M, Wang J, Zhong X, *et al*: The role of mitochondria in the resistance of melanoma to PD-1 inhibitors. J Transl Med 21: 345, 2023.
14. Huang AC and Zappasodi R: A decade of checkpoint blockade immunotherapy in melanoma: Understanding the molecular basis for immune sensitivity and resistance. Nat Immunol 23: 660-670, 2022.
15. Jenkins RW, Barbie DA and Flaherty KT: Mechanisms of resistance to immune checkpoint inhibitors. Br J Cancer 118: 9-16, 2018.
16. Tang Q, Chen Y, Li X, Long S, Shi Y, Yu Y, Wu W, Han L and Wang S: The role of PD-1/PD-L1 and application of immune-checkpoint inhibitors in human cancers. Front Immunol 13: 964442, 2022.
17. Zak KM, Grudnik P, Magiera K, Dömling A, Dubin G and Holak TA: Structural biology of the immune checkpoint receptor PD-1 and its ligands PD-L1/PD-L2. Structure 25: 1163-1174, 2017.
18. Zong WX, Rabinowitz JD and White E: Mitochondria and cancer. Mol Cell 61: 667-676, 2016.
19. Kuntz EM, Baquero P, Michie AM, Dunn K, Tardito S, Holyoake TL, Helgason GV and Gottlieb E: Targeting mitochondrial oxidative phosphorylation eradicates therapy-resistant chronic myeloid leukemia stem cells. Nat Med 23: 1234-1240, 2017.
20. Yamashita K, Kinoshita M, Miyamoto K, Namba A, Shimizu M, Koda T, Sugimoto T, Mori Y, Yoshioka Y, Nakatsuji Y, *et al*: Cerebrospinal fluid mitochondrial DNA in neuromyelitis optica spectrum disorder. J Neuroinflammation 15: 125, 2018.
21. Cheng AN, Cheng LC, Kuo CL, Lo YK, Chou HY, Chen CH, Wang YH, Chuang TH, Cheng SJ and Lee AY: Mitochondrial Lon-induced mtDNA leakage contributes to PD-L1-mediated immunoescape via STING-IFN signaling and extracellular vesicles. J Immunother Cancer 8: e001372, 2020.
22. Gerasimov ES, Gasparyan AA, Kaurov I, Tichý B, Logacheva MD, Kolesnikov AA, Lukeš J, Yurchenko V, Zimmer SL and Flegontov P: Trypanosomatid mitochondrial RNA editing: Dramatically complex transcript repertoires revealed with a dedicated mapping tool. Nucleic Acids Res 46: 765-781, 2018.
23. Knapek KJ, Georges HM, van Campen H, Bishop JV, Bielefeldt-Ohmann H, Smirnova NP and Hansen TR: Fetal lymphoid organ immune responses to transient and persistent infection with bovine viral diarrhea virus. Viruses 12: 816, 2020.
24. Miao Z, Tian W, Ye Y, Gu W, Bao Z, Xu L, Sun G, Li C, Tu Y, Chao H, *et al*: Hsp90 induces Acsl4-dependent glioma ferroptosis via dephosphorylating Ser637 at Drp1. Cell Death Dis 13: 548, 2022.
25. Rinwa P, Eriksson M, Cotgreave I and Bäckberg M: 3R-Refinement principles: Elevating rodent well-being and research quality. Lab Anim Res 40: 11, 2024.
26. Guan S, Zhao L and Peng R: Mitochondrial respiratory chain supercomplexes: From structure to function. Int J Mol Sci 23: 13880, 2022.
27. Newton K, Strasser A, Kayagaki N and Dixit VM: Cell death. Cell 187: 235-256, 2024.
28. Yi M, Zheng X, Niu M, Zhu S, Ge H and Wu K: Combination strategies with PD-1/PD-L1 blockade: Current advances and future directions. Mol Cancer 21: 28, 2022.
29. Li X, Liu Y, Gui J, Gan L and Xue J: Cell identity and spatial distribution of PD-1/PD-L1 blockade responders. Adv Sci (Weinh) 11: e2400702, 2024.
30. Yu Y, Peng XD, Qian XJ, Zhang KM, Huang X, Chen YH, Li YT, Feng GK, Zhang HL, Xu XL, *et al*: Fis1 phosphorylation by Met promotes mitochondrial fission and hepatocellular carcinoma metastasis. Signal Transduct Target Ther 6: 401, 2021.
31. Wong YC, Ysselstein D and Krainc D: Mitochondria-lysosome contacts regulate mitochondrial fission via RAB7 GTP hydrolysis. Nature 554: 382-386, 2018.
32. Opstad IS, Godtliebsen G, Ahluwalia BS, Myrmel T, Agarwal K and Birgisdottir ÅB: Mitochondrial dynamics and quantification of mitochondria-derived vesicles in cardiomyoblasts using structured illumination microscopy. J Biophotonics 15: e202100305, 2022.
33. Harel M, Ortenberg R, Varanasi SK, Mangalhara KC, Mardamshina M, Markovits E, Baruch EN, Tripple V, Arama-Chayoth M, Greenberg E, *et al*: Proteomics of melanoma response to immunotherapy reveals mitochondrial dependence. Cell 179: 236-250.e18, 2019.
34. Klein K, He K, Younes AI, Barsoumian HB, Chen D, Ozgen T, Mosaffa S, Patel RR, Gu M, Novaes J, *et al*: Role of mitochondria in cancer immune evasion and potential therapeutic approaches. Front Immunol 11: 573326, 2020.
35. Porporato PE, Filigheddu N, Pedro JMB, Kroemer G and Galluzzi L: Mitochondrial metabolism and cancer. Cell Res 28: 265-280, 2018.

36. Ye L, Wen X, Qin J, Zhang X, Wang Y, Wang Z, Zhou T, Di Y and He W: Metabolism-regulated ferroptosis in cancer progression and therapy. Cell Death Dis 15: 196, 2024.
37. Halma MTJ, Tuszynski JA and Marik PE: Cancer metabolism as a therapeutic target and review of interventions. Nutrients 15: 4245, 2023.
38. Vander Heiden MG, Lunt SY, Dayton TL, Fiske BP, Israelsen WJ, Mattaini KR, Vokes NI, Stephanopoulos G, Cantley LC, Metallo CM and Locasale JW: Metabolic pathway alterations that support cell proliferation. Cold Spring Harb Symp Quant Biol 76: 325-334, 2011.
39. Chatterjee R and Chatterjee J: ROS and oncogenesis with special reference to EMT and stemness. Eur J Cell Biol 99: 151073, 2020.
40. Moloney JN and Cotter TG: ROS signalling in the biology of cancer. Semin Cell Dev Biol 80: 50-64, 2018.
41. Yang Y, Karakhanova S, Hartwig W, D'Haese JG, Philippov PP, Werner J and Bazhin AV: Mitochondria and mitochondrial ROS in cancer: Novel targets for anticancer therapy. J Cell Physiol 231: 2570-2581, 2016.
42. DeBerardinis RJ and Chandel NS: Fundamentals of cancer metabolism. Sci Adv 2: e1600200, 2016.
43. Missiroli S, Perrone M, Genovese I, Pinton P and Giorgi C: Cancer metabolism and mitochondria: Finding novel mechanisms to fight tumours. EBioMedicine 59: 102943, 2020.